PHYSICAL REVIEW E **95**, 060901(R) (2017)

Universality in quasi-two-dimensional granular shock fronts above an intruder

M. Yasinul Karim and Eric I. Corwin
Materials Science Institute and Department of Physics, University of Oregon, Eugene, Oregon 97403, USA
(Received 24 January 2017; published 23 June 2017)

We experimentally study quasi-two-dimensional dilute granular flow around intruders whose shape, size, and relative impact speed are systematically varied. Direct measurement of the flow field reveals that three in-principle independent measurements of the nonuniformity of the flow field are in fact all linearly related: (1) granular temperature, (2) flow-field divergence, and (3) shear-strain rate. The shock front is defined as the local maxima in each of these measurements. The shape of the shock front is well described by an inverted catenary and is driven by the formation of a dynamic arch during steady flow. We find universality in the functional form of the shock front within the range of experimental values probed. Changing the intruder size, concavity, and impact speed only results in a scaling and shifting of the shock front. We independently measure the horizontal lift force on the intruder and find that it can be understood as a result of the interplay between the shock profile and the intruder shape.

DOI: 10.1103/PhysRevE.95.060901

Lift forces [1–4] on and shock formation [5–7] around intruders in granular flows are well-known phenomena. Rericha *et al.* [6] and Boudet *et al.* [8,9] have demonstrated that shocks analogous to those in fluid flows are formed around symmetrical intruders in dilute granular flows. Numerical studies by Potiguar [3] have shown that in the case of asymmetrical intruders, the drag-induced lift forces are lower than expected due to the formation of shock waves that act as a shield. However, the relationship between the granular shock front and lift (forces perpendicular to the direction of flow) on an intruder needs to be studied in detail.

In this Rapid Communication, we systematically vary the shape of an intruder in a dilute granular flow and measure the resulting grain flow fields and lift forces. We find that the position of the shock front is well described by each of the coordinates of the local maxima of granular temperature, divergence, and local shear-strain rate, which are all found to be linearly related. The shock front maintains a symmetric shape and its center point closely tracks the center of mass of the intruder. We find that the asymmetry of the intruder alters the shock boundary and this in turn alters the lift force on the intruder. We propose a model for calculating lift forces which agrees with experimental data. We demonstrate that the force in the direction perpendicular to flow is the result of three mechanisms: (1) static loading from the dead zone above the intruder, (2) impact forces from the freely falling grains hitting the shock front, and (3) net momentum transfer due to mass ejection from the dead zone.

Our experimental setup consists of a rectangular quasi-two-dimensional (2D) granular hopper that is 1.25 cm deep, 55.8 cm wide, and 90 cm in height. The hopper is constructed from $\frac{1}{4}$-in. acrylic, as shown in Fig. 1(a). The front of the hopper is clear and the back is opaque to allow for quantitative imaging of the flow. The hopper is fed by a reservoir of 3-mm glass beads (Mo-Sci Corporation) to provide a steady flow rate of approximately 400 particles $\mathrm{cm}^{-2}\,\mathrm{s}^{-1}$. A laser-cut acrylic intruder is placed inside the hopper and is constructed to be 1.1 cm thick, slightly thinner than the hopper cavity to prevent frictional contact with the front and back walls. The intruder is typically mounted at $h = 57$ cm below the reservoir, where the bead velocity in the absence of the intruder would be $v_0 = 3.3$ m/s, comparable to the flow speeds in Refs. [6,7,10]. Changing h corresponds to changing the impact speed v_0 of the grains, $v_0 \propto \sqrt{h}$.

Figure 1(b) shows the intruder-sensor system. The intruder is connected to one end of a 30-cm aluminum rod. The other end of the rod is held in place by a force sensor to measure lateral forces (Measurement Specialties FC22) and a preload which is subtracted from the measurements. This is fixed to a second rod to form a T-shaped structure which is held by low friction bearings.

The intruder shape is defined as the first quadrant of the superdisk equation [11]

$$y = (1 - x^n)^{\frac{1}{n}}, \tag{1}$$

where x and y are the horizontal and vertical coordinates. The exponent n controls the concavity and symmetry of the shape, as illustrated by the six shapes in Fig. 1(c). The superdisk equation provides a family of shapes interpolating from the asymmetric "L" at $n = 0$ to a triangle at $n = 1$, a quarter circle at $n = 2$, and a square at $n = \infty$. Unless otherwise specified, the length R of the straight edge is held constant at 4 in.

At the beginning of each measurement the bottom of the hopper is blocked off and it is filled with beads. When the beads are released the force sensor and a high-speed camera (Phantom M310) start recording. We ignore the initial transient (approximately 0–4 s) when beads begin to flow and keep only the measurements taken in the steady state—when the flow rate is roughly constant. After about 10 s the reservoir is depleted.

For each value n we measure lateral forces on, and granular flow field around, the intruder. Bead velocities are calculated using particle image velocimetry (PIV) [12]. In agreement with previous studies [8,13–17], in steady-state flow we observe a nearly stationary, densely packed pile of beads with a shock front above the leading edge of the intruder. This shock front can be identified by three different measurements: the local maxima of granular temperature T, flow divergence f_d, and shear-strain rate $\dot{\gamma}$,

$$T = \langle \vec{v} \cdot \vec{v} \rangle - \langle \vec{v} \rangle \cdot \langle \vec{v} \rangle, \tag{2}$$

$$f_d = |\nabla \cdot \vec{v}|, \tag{3}$$

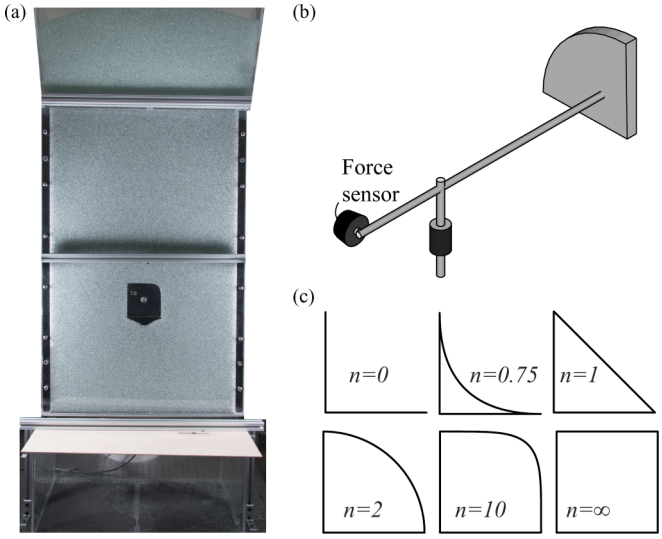

FIG. 1. (a) Front view of experimental setup. The intruder in the picture corresponds to a superdisk exponent $n = 7.5$. (b) Intruder-sensor system schematic. (c) Examples of intruders with different superdisk exponents. As n increases, the shapes become more convex, with $n = \infty$ being a square.

and

$$\dot{\gamma} = (d_1 - d_2)/2, \tag{4}$$

where $\vec{v}$ is the velocity at any given point. Angle brackets denote time averages and d_1 and d_2 are eigenvalues of the strain rate tensor $\mathbf{D} = \nabla\vec{v} + (\nabla\vec{v})^{\mathbf{T}}$, following the method described by Clark *et al.* [10].

For all values of n, these three tests pick out the same feature above the intruder. They are shown for a representative intruder with $n = 0.75$ in Figs. 2(a)–2(c). These quantities are all close to zero everywhere else in the flow field. By picking out only the points inside the same dotted regions in Figs. 2(a)–2(c), we plot divergence versus temperature, divergence versus shear rate, and shear rate versus temperature in Figs. 2(d)–2(f), respectively. We nondimensionalize these quantities by scaling them as T/v_0^2, $(d/v_0)|\nabla\cdot\vec{v}|$, and $(d/v_0)\dot{\gamma}$, where v_0 is the theoretical free-fall speed of beads at the intruder's center of mass and d is the bead diameter. In Fig. 2(e) the red dotted line corresponds to a slope of 2. Since $|f_d| = |d_1 + d_2|$ and $\dot{\gamma} = d_1 - d_2$, where d_1 and d_2 are eigenvalues of the shear-strain tensor, Fig. 2(e) shows that $|d_1 + d_2| > \frac{1}{2}(d_1 - d_2)$. The points in the scatter plot fall below the slope $= 2$ line [red dotted line in Fig. 2(e)] showing that $d_1 \gg d_2$.

The nonzero divergence band is a region of high compressibility—grains suddenly decelerate upon impact and some get absorbed into the quasistatic pile on the intruder. The same band also displays high variance in the velocity field due to sudden grain-grain collisions and consequent velocity changes. The linear relationship between the three measured quantities are unexpected and remain to be studied further in a future study.

Figure 3(a) shows the extracted shock front for intruders of varying n. The plots show that the shock front maintains the same functional form as the intruder geometry is varied, with the curves shifting right and increasing in peak height with increasing n. For any given obstacle shape we find that the volume of trapped beads remains constant. Volume fluctuations are low so we assume a system with negligible dilatancy and bounded by a shock front that prefers to maintain a shape dictated by force constraints.

During steady-state flow the shock front must remain stable. Any vertical or horizontal net force will result in a time variant shock front. To enforce stability of the archlike shock front given the constraints of gravity, the net force must be tangential to the surface of the shock, as illustrated by the green arrow in Fig. 5(a) (inset). This net force ensures that particles not absorbed by the quasistatic pile are cleared away from it such that the shock front remains stable. The ejection of particles from the left and right, illustrated by purple arrows in Fig. 5(a) (inset), also ensures a stable shock position during steady flow.

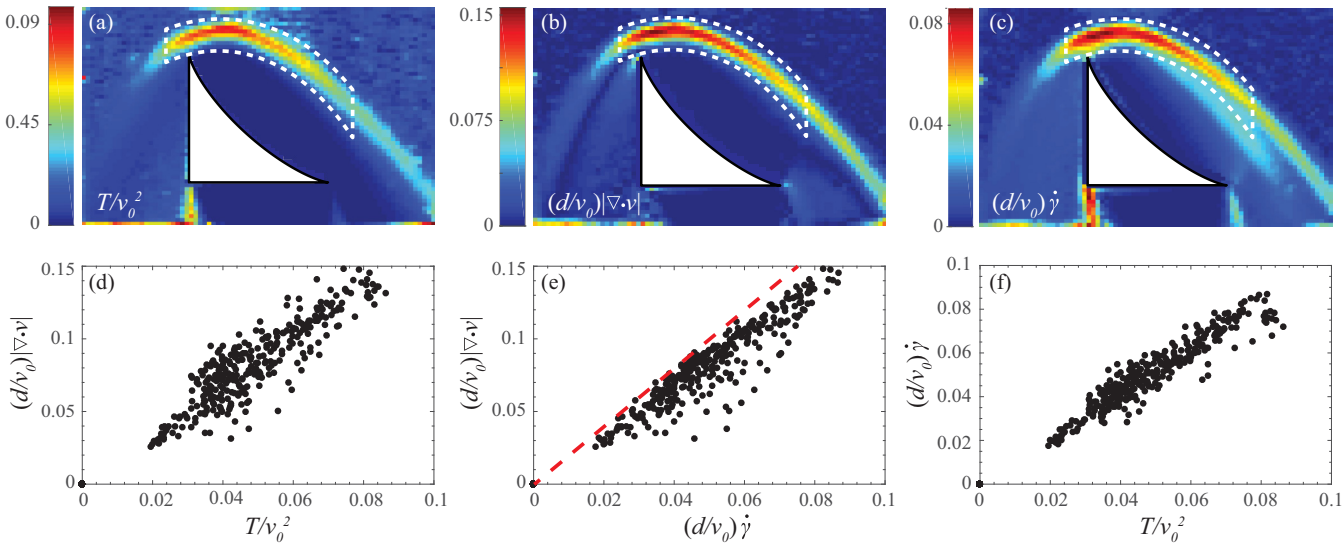

FIG. 2. (a)–(c) Intensity plot of scaled granular temperature, absolute divergence of the flow field, and local shear-strain rate for $n = 0.75$. (d)–(f) Scatter plots of scaled flow-field divergence vs temperature, flow-field divergence vs local shear rate, and shear rate vs temperature, respectively, measured from all points enclosed by the white dotted regions.

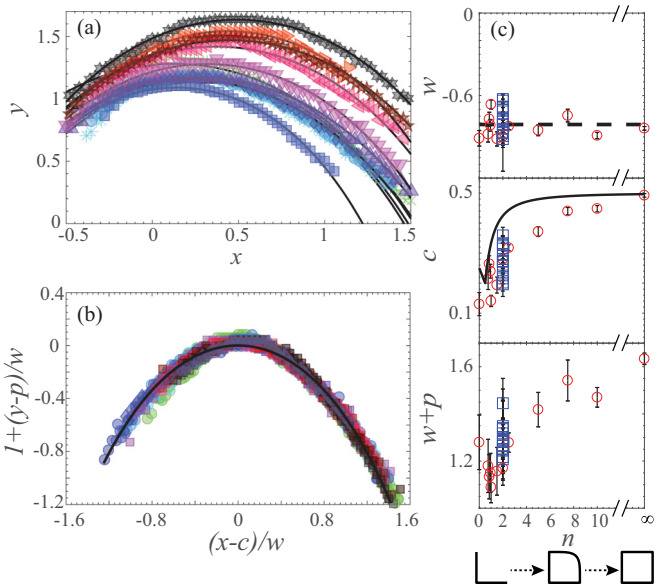

FIG. 3. (a) Plots of shock fronts. Scaled x and y coordinates are in units of R, the vertical length of the intruder. The data are shown for $n = 0$ (+), 0.75 (×), 0.85 (∗), 0.95 (○), 1 (□), 1.5 (◊), 2 (△), 2.5 (▽), 5 (◁), 7.5 (▷), 10 (☆), ∞ (✡). Solid black lines are fits to Eq. (7). (b) Plot of scaled shock boundaries for all probed values of n with constant $R = 4$ in., shown in circles. Squares represent all tested intruder locations $h \in \{23,34,46,57,69,84\}$ cm and intruder radii $R \in \{2,3,4,7\}$ in. for constant $n = 2$. Diamond symbols represent data from an asymmetric intruder with random features on it, as shown in Fig. 4. The black curve is the inverted catenary given by Eq. (7). (c) Top to bottom: Plots of the fit parameters w, c, and $w + p$ as functions of n, respectively. Red circles represent data from varying n with constant R and blue squares represent data from fixed $n = 2$ but different combinations of R and impact speed v_0. The dashed line shows the mean width $|\bar{w}| \approx 0.8$. In the c vs n plot, the dark solid curve shows the center of mass of the intruders shifts with varying n.

Force balance also implies that the ith particle in the quasistatic layer is held in place at an angle of repose θ_i such that $K_i\mu = \tan\theta_i$, where μ is the coefficient of friction and K_i is a friction mobilization factor at the ith location. Thus, $\tan\theta_i = \frac{\Delta y_i}{\Delta x_i}$.

We define s_i as the arc length spanning the horizontal distance l, the particle diameter. For a convex shock profile the ratio s_i/l is an approximate measure of K_i. A higher ratio implies more friction mobilized to constrain the particle. When the tangent to s_i is horizontal, $\tan\theta_i = 0$ and $s_i/l = 1$. To enforce this condition we assume that to first order $K_i \propto (s_i/l - 1)$. In the discrete limit, for some constant of proportionality C,

$$\left(\frac{s_i}{l} - 1\right) C\mu = \tan\theta_i = \frac{\Delta y_i}{\Delta x_i}. \tag{5}$$

In the continuum limit, taking the x derivative on both sides of Eq. (5),

$$(C\mu/l)\frac{ds}{dx} = \frac{1}{w}\frac{ds}{dx} = \frac{d^2y}{dx^2}. \tag{6}$$

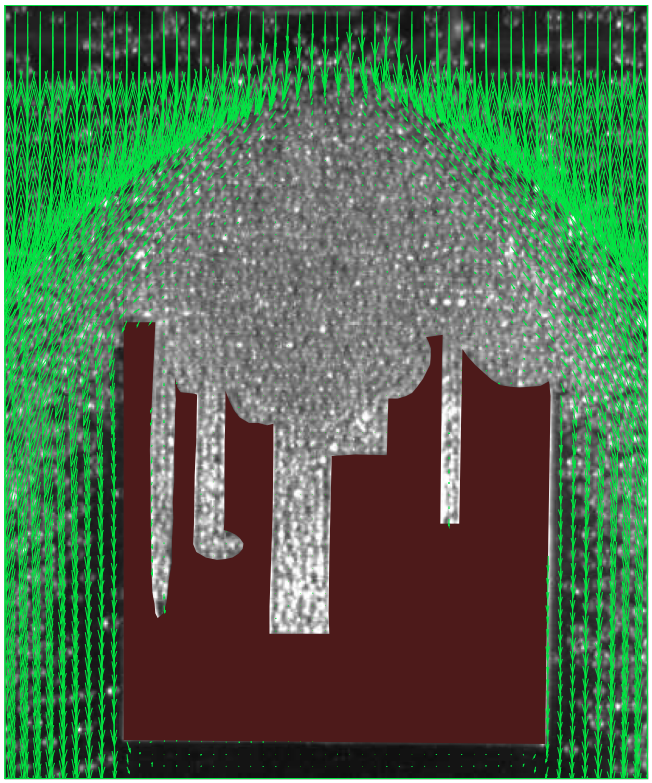

FIG. 4. Representative mean flow field around an intruder with no line of symmetry. The masked out region is the intruder and the arrows are velocity vectors calculated from PIV.

Equation (6) has the solution

$$y = w\cosh\left(\frac{x - c}{w}\right) + p. \tag{7}$$

Equation (7) is an inverted catenary where $|w|$ is the characteristic width of the hyperbolic cosine curve, c sets the center of the curve, and p is the vertical offset such that $y(x = c) = w + p$. Surprisingly, this description of the shock front has the same solution as the shape of an arch in a jammed pipe [18].

The measured shock fronts are well fit by Eq. (7), as demonstrated by the dark lines in Fig. 3(a). Thus we find that in steady granular flow the shock front (ignoring temporal fluctuations) is a dynamic arch. By scaling out the fit parameters we find an excellent collapse onto a single master curve, as demonstrated in Fig. 3(b). This indicates that the influence of the intruder shape is limited to changing the center point and height of the resulting shock wave.

To test the effect of intruder size R for a superdisk exponent $n = 2$, we measured several combinations of varying R and height h. Figure 3(b) includes measurements for all probed values of n and all tested combinations (R,h) for $n = 2$. This provides strong evidence for the universality of the shape of the shock front; varying any of the parameters, intruder shape n, intruder size R, and impact or incident grain velocity v_0, does not change the shape of the shock front. Finally, we created an intruder with no obvious symmetry, shown in Fig. 4, and found that its shock front, plotted as diamonds in Fig. 3(b), also collapses to the same master curve.

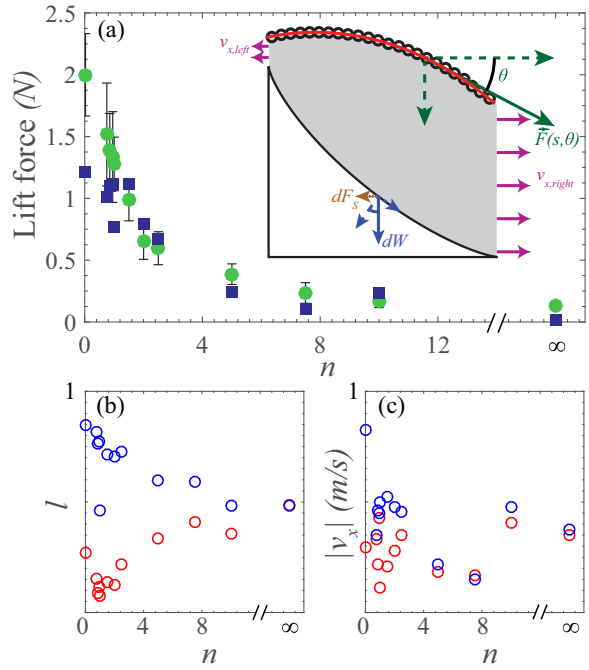

FIG. 5. (a) Plot of horizontal lift forces from force sensor (green circle) and calculated lift forces (dark blue squares) as a function of n. Lift is maximum for $n \to 0$ and decreases to 0 as $n \to \infty$. The inset is an illustration showing the intruder, outlined in black, trapped grains in gray, and the shock profile in red. The solid green arrow represents the tangential net force $\vec{F}(s,\theta)$ on a small segment of the shock front. Dotted green arrows are components of this vector. Purple arrows labeled $v_{x,0/1}$ represent horizontal ejected grain velocities from the trapped region. (b) Plot of the left (red) and right (blue) exit heights l as a function of n. (c) Plot of absolute horizontal left (red) and right (blue) exit velocities $|v_x|$ vs n.

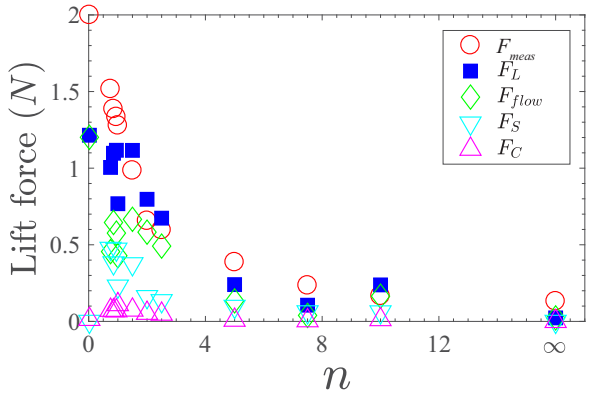

FIG. 6. Plots of total measured lift force F_{meas}, calculated lift force F_L (blue squares), force due to mass ejection from trapped pile F_{flow} (green diamond), quasistatic load contribution F_S (downward pointing arrow), and force due to impacts F_C (upward pointing arrow) as a function of n.

We obtain the constants w, c, and p as fit parameters to Eq. (7) and plot them as functions of n in Fig. 3(c), where red circles represent data for varying n and blue squares represent data for different combinations (R,h) for $n = 2$. The plot of width w vs n demonstrates that the scaled width of the catenary is independent of the shape parameter n and the dotted line denotes the mean value -0.8 of the curve width. The plot of center c vs n agrees with the qualitative observation from Fig. 3(a)—the peaks shift away from the vertical edge as n goes from $0 \to \infty$. The center naturally asymptotes to $c = 0.5$ for $n \to \infty$ as the shape of the intruder approaches a symmetric square. We find that c roughly tracks the intruder center of mass (black solid curve). Plotting $y(x = c)$, which is the peak height $w + p$, as a function of n demonstrates that the peaks shift upwards with increasing n. Thus, we find that the intruder shape parameter n controls the catenary center and peak.

The shape of the catenary affects how grains are distributed on the intruder and thus, in turn, determines the lift forces F_L. We show this by directly measuring F_L, the lift force perpendicular to the direction of flow, on the intruder. The measured lift as a function of n is plotted as green circles in Fig. 5(a). The lift is maximum for $n = 0$, and decreases with increasing n and asymptotes to 0 as $n \to \infty$, in which case the intruder is perfectly symmetric. We describe the lift force F_L by a simple model consisting of three parts: the horizontal component of the static load F_S, the horizontal component of the impact forces F_C, and the horizontal forces due to momentum transfer of outflowing particles F_{flow}.

The first contribution is from the horizontal component dF_S of the static load W pushing on the curved upper surface of the intruder. For all intruder shapes there is a quasistatic trapped mass bounded above by the shock front. Because this mass is resting on a curved, asymmetric surface, it will impart a nonzero horizontal component F_S. In the limiting cases $n = 0$ or ∞ this contribution goes to zero.

This quasistatic pile has a mass proportional to the volume enclosed by the shock front and the intruder profile, represented by the gray region in Fig. 5(a) (inset). For a given exponent n, the shape of the intruder profile is given by $g(x) = (1 - x^n)^{1/n}$ [derived from Eq. (1)] and the shock front $f(x)$ given by Eq. (7). For a small segment of the trapped area of width dx and thickness w_{cell}, the volume $dV = w_{\text{cell}}[f(x) - g(x)]dx$. The net horizontal component of this weight is given by

$$F_S = \int_0^1 w_{\text{cell}}[f(x) - g(x)]\phi\rho_g g \cos[\alpha(x)] \sin[\alpha(x)]dx, \tag{8}$$

where the density of glass is $\rho_g = 2500\ \text{kg/m}^3$, g is the gravitational acceleration, and $\alpha(x)$ the angle between the horizontal and tangent to $g(x)$. We approximate the volume fraction $\phi = 0.6$, slightly lower than random close packing to account for the presence of confining walls, which is about eight bead diameters thick. The cosine term gives the normal component to the tangent and the sine resolves the horizontal component. The horizontal component is integrated over the length of the intruder to calculate the lift force due to the static pack. The integration limits are $x \in [0,1]$, where $x = 0$ and $x = 1$ are the left and right edges of the intruder, respectively. Figure 6 shows the measured (F_{meas}) and calculated (F_L) force and its components F_S, F_C, and F_{flow}.

The second force contribution is from the momentum flux of freely falling particles impacting the shock front. This force, F_C, is equal to the incident mass per unit time perpendicular

to the shock front multiplied by the velocity change in the horizontal direction. The incident velocities along the shock front are taken from PIV measurements.

The collisional force F_C due to beads impacting the shock boundary is given by

$$F_C = \int_0^1 \phi_d \rho_g w_{\text{cell}} [\vec{v}(x) \cdot \hat{n}(x)]^2 \sin\theta(x) dx, \tag{9}$$

where $\phi_d \rho_g w_{\text{cell}} \vec{v}(x) \cdot \hat{n}(x) dx$ is the incident mass per unit time at x on a small segment dx of the shock front. $\theta(x)$ is the angle between the horizontal and tangent to $f(x)$. The normal component of the incident velocity of particles colliding with the shock front is given by $\vec{v}(x) \cdot \hat{n}(x)$. The fraction of space occupied by freely falling particles is $\phi_d \approx 0.03$, as measured directly from the images. Assuming that collisions are inelastic, the rate of momentum transfer normal to $f(x)$ is $\phi_d \rho_g w_{\text{cell}} [\vec{v}(x) \cdot \hat{n}(x) dx][\vec{v}(x) \cdot \hat{n}(x)] \sin\theta(x)$. The sine term in Eq. (9) comes from the horizontal component of this force at $g(x)$. As Fig. 6 shows, F_C (upward pointing arrows) accounts for the lowest contribution to the calculated force.

The third force contribution F_{flow} is from grains being ejected from the area between the shock front and the intruder profile. These grains are measured to leave with average speeds $v_{x,\text{left}}$ and $v_{x,\text{right}}$ illustrated by purple arrows in Fig. 5(a) (inset). Since we keep the width of the hopper constant, the scaled heights l_{left} and l_{right}, distances from the intruder to the shock front at $x = 0$ (red circles) and $x = 1$ (blue circles), respectively, are measures of the exit areas. The distances $l_{\text{left/right}}$ are plotted as functions of n in Fig. 5(b) and are scaled by the intruder size R as before. We find that the difference in the two exit areas ($|l_{\text{left}} - l_{\text{right}}|$) decreases with increasing n and becomes equal at $n = \infty$. This implies that for equal exit velocities more grains can escape from the exit area at $x = 1$, which in turn means greater momentum flux at this edge.

This reaction force F_{flow} on the intruder due to mass ejection from the granular pile is given by

$$F_{\text{flow}} = \phi\rho w_{\text{cell}} \left([f(1) - g(1)] v_{x,1}^2 - [f(0) - g(0)] v_{x,0}^2 \right), \tag{10}$$

where $\phi\rho w_{\text{cell}} (f(x_0) - g(x_0)) v^2$ is the horizontal momentum transferred due to particles being ejected from the area between $f(x_0)$ and $g(x_0)$. The velocities $v_{x,0}$ and $v_{x,1}$ are the mean horizontal bead velocities exiting the cross section $w_{\text{cell}}[f(x) - g(x)]$ at $x = 0$ and $x = 1$, respectively. The volume fraction is $\phi = 0.6$. As Fig. 6 shows, F_{flow} accounts for the highest contribution to F_L in our model.

The mean exit velocities at $x = 0$ (red circles) and $x = 1$ (blue circles) obtained from PIV measurements are plotted in Fig. 5(c) and we find that the speeds are roughly the same and nearly equal for $n > 2$. Thus, for asymmetrical intruders the disparity in granular exit areas becomes the dominating factor. At smaller n, as the shape becomes more concave and asymmetric, the momentum flux on the right at $x = 1$ is greater, so F_{flow} is higher. For larger values of n, the two areas and speeds are comparable, so the net momentum flux F_{flow} approaches zero for $n \to \infty$.

Our approach to calculating lift is similar to the granular resistive force theory technique (GRFT) pioneered by Zhang and Goldman [19] and further explained by Askari and Kamrin [20]. While GRFT has been effective in predicting and modeling dynamics in friction-dominated granular systems [21], Zhang and Goldman conclude that GRFT may not be applicable when inertial forces dominate [19]. Our results demonstrate this is indeed the case in such systems; the inertial forces cannot be ignored when computing net lift, for instance. In dilute granular flows further complications arise due to the separation of grains into a solidlike and fluidlike region.

This experiment reveals that in the region near the granular shock front the mean flow-field variance, absolute flow-field divergence, and shear-strain rate are linearly related to each other. The local maxima in each of these measurements provide a robust means of identifying the shock front. The shock front is characterized by a universal functional form that is, unlike the fluid flow analog, invariant with respect to intruder size, shape, and impact speeds within probed experimental values. To enforce stability given the constraints of gravity and granular impact forces, there must always be a tangential force along the shock front. This leads to an appropriate organization of quasistatic grains around the intruder such that the effective shape becomes archlike and well described by an inverted catenary. The catenary center lines ($x = c$) roughly track the intruders' centers of mass ($x = x_m$). The two lines begin to converge as the intruder approaches a more symmetrical shape. Variation in intruder geometry results in scaling and shifting of the catenary and this determines the lift force on the intruder. We also demonstrate that the mechanism for lift in dilute granular flows consists of at least three processes rather than just collisional forces, as might be naively expected.

In dilute flows, the quasistatic granular pack is analogous to a hydrodynamic radius and determines the effective shape of an intruding object. The existence of several measurements to identify the shock boundary and universality in its shape should pave the way for a better understanding of boundary conditions and more refined applications of Navier-Stokes-like continuum models to dilute granular flows. Our work also presents avenues for future exploration of drag forces on intruder shape, size, and impact speeds. This future work would further detail the extent to which granular lift is drag induced.

We acknowledge support from the National Science Foundation (NSF) Career Award DMR-1255370 and the Simons Foundation Grant No. 454939.

[1] R. Soller and S. A. Koehler, Phys. Rev. E **74**, 021305 (2006).
[2] Y. Ding, N. Gravish, and D. I. Goldman, Phys. Rev. Lett. **106**, 028001 (2011).
[3] F. Q. Potiguar, Phys. Rev. E **84**, 061302 (2011).
[4] F. Q. Potiguar and Y. Ding, Phys. Rev. E **88**, 012204 (2013).
[5] P. K. Haff, J. Fluid Mech. **134**, 401 (1983).
[6] E. C. Rericha, C. Bizon, M. D. Shattuck, and H. L. Swinney, Phys. Rev. Lett. **88**, 014302 (2001).

[7] Y. Amarouchene and H. Kellay, Phys. Fluids **18**, 031707 (2006).
[8] J. F. Boudet, Y. Amarouchene, and H. Kellay, Phys. Rev. Lett. **101**, 254503 (2008).
[9] J. F. Boudet and H. Kellay, Phys. Rev. Lett. **105**, 104501 (2010).
[10] A. H. Clark, L. Kondic, and R. P. Behringer, Phys. Rev. E **93**, 050901 (2016).
[11] Y. Jiao, F. H. Stillinger, and S. Torquato, Phys. Rev. E **79**, 041309 (2009).
[12] W. Thielicke and E. Stamhuis, J. Open Res. Software **2**, e30 (2014).
[13] Y. Amarouchene, J. F. Boudet, and H. Kellay, Phys. Rev. Lett. **86**, 4286 (2001).
[14] C. R. Wassgren, J. A. Cordova, R. Zenit, and A. Karion, Phys. Fluids **15**, 3318 (2003).
[15] P. Knoll, S. Mirzaei, and H. Köhn, Appl. Math. Comput. **190**, 1747 (2007).
[16] J. K. Meyer and R. L. Merlino, Phys. Plasmas **20**, 074501 (2013).
[17] A. Vilquin, J. F. Boudet, and H. Kellay, Phys. Rev. E **94**, 022905 (2016).
[18] C. C. Mounfield and S. F. Edwards, Physica A (Amsterdam) **226**, 12 (1996).
[19] T. Zhang and D. I. Goldman, Phys. Fluids **26**, 101308 (2014).
[20] H. Askari and K. Kamrin, Nat. Mater. **15**, 1274 (2016).
[21] J. Aguilar, T. Zhang, F. Qian, M. Kingsbury, B. McInroe, N. Mazouchova, C. Li, R. Maladen, C. Gong, M. Travers, R. L. Hatton, H. Choset, P. B. Umbanhowar, and D. I. Goldman, Rep. Prog. Phys. **79**, 110001 (2016).